Received: 15 May 2023 | Revised: 22 October 2023 | Accepted: 25 October 2023

DOI: 10.1111/jace.19542

Journal of the American Ceramic Society

RESEARCH ARTICLE

Environmental conical nozzle levitator equipped with dual wavelength lasers

Fox Thorpe[1] | **Trevor Li**[2] | **Richard Weber**[3] | **Scott J. McCormack**[2]

[1]Department of Chemical Engineering, University of California, Davis, California, USA

[2]Department of Materials Science and Engineering, University of California, Davis, California, USA

[3]Materials Development Inc., Evanston, Illinois, USA

Correspondence
Scott J. McCormack, Department of Materials Science and Engineering, University of California, Davis, CA 95616, USA.
Email: sjmccormack@ucdavis.edu

Funding information
National Science Foundation; Directorate for Mathematical and Physical Sciences; Division of Materials Research; Ceramic, Grant/Award Number: 2047084

Abstract

The environmental conical nozzle levitator (E-CNL) with dual-wavelength lasers is an extreme environment materials characterization system that was designed to investigate ultra-high-temperature materials: refractory metals, oxides, carbides, and borides above 3000 K in a controlled atmosphere. This article details the characterizations using this system to establish its high-temperature capabilities and to outline ongoing work on materials under extreme conditions. The system has been used to measure the melting point of several oxide materials (TiO_2, Tm = 2091 ± 3 K; Al_2O_3, Tm = 2310 ± 3 K; ZrO_2, Tm = 2984 ± 31 K; and HfO_2, Tm = 3199 ± 45 K) and several air-sensitive refractory metals (Ni, Tm = 1740 ± 10 K; Ti, Tm = 1983 ± 16 K; Nb, Tm = 2701 ± 12 K; and Ta, Tm = 3368 ± 24 K—note: mean ± standard deviation) during levitation which matched literature values within 0.17–2.43 % demonstrating high accuracy and precision. This containerless measurement approach is critical for probing properties without container-derived contamination, and dual-wavelength laser heating is essential to heat both relatively poor electrical conductors (some refractory metals and carbides) and insulators (oxides). The highest temperature achieved utilizing both lasers in these experiments was ~4250 ± 34 K on a 76.6 mg, molten HfO_2 sample using a normal spectral emissivity of 0.91. Stable levitation was demonstrated on spherical samples (yttria-stabilized zirconia) while adjusting levitation gas composition from pure oxygen to pure argon, verifying atmospheric control up to 3173 K on solid or molten samples. These successes demonstrate the viability of in situ high-temperature environmentally controlled studies potentially up to 4000 K on all classes of ultra-high-temperature materials in one system. These measurements highlight the E-CNL system will be essential for the development of next-generation ultra-high-temperature materials for hypersonic platforms, nuclear fission and fusion, and space exploration.

KEYWORDS
ceramics, high temperature, melting point, metals, refractory, ultra-high-temperature materials

---

1 | INTRODUCTION

The future of many aspects of technology will require new ultra-high temperature ceramics (UHTCs): materials with operating temperatures above 2273 K.[1,2] Travel within our solar system will require next-generation heat shields that can withstand both high temperatures and highly reactive environments. For example, re-entry temperatures on Mars and Venus are estimated to be ∼1573 K[3] and ∼3023 K[4] respectively; atmosphere will add to the burden of the heat shield materials. Re-entry temperatures experienced on Earth can reach temperatures of ∼ 2273 K.[5] Future propulsion systems will require operating temperatures up to ∼2700 K,[6] such as Nuclear Thermal Propulsion (NTP) systems,[7] which will reduce travel time to Mars from Earth by ∼75%. Conventional propulsion, like that used for the perseverance 2020 mission, took ∼200 days[8] compared with the proposed NTP which would take ∼45 days.[9] Future energy systems required to fuel life on Earth will require materials to operate up to ∼1800 K. The very high-temperature reactor (VHTR), a fourth-generation nuclear reactor, will operate at ∼1773 K.[10] Fusion reactors[11] will require materials to operate above 1573 K while being exposed to fast neutron energy on the order of 14 MeV.[12]

Research on UHTCs is hampered by two factors: (1) unwanted chemical reactions that interfere with processing, and (2) difficulty heating them to the temperatures of interest. An additional practical issue is the measurement of temperatures above ∼3000 K and the lack of high-temperature materials emissivity data in the literature.

Thus, to design engineering materials to operate in these extreme environments, engineers, and scientists need access to high-temperature materials diagnostic tools. This led to the development and utilization of high-temperature graphite furnaces that heat samples up to ∼3273 K. These systems can be coupled with mechanical testing[13–16] and dilatometry[17,18] along with other materials diagnostic measurements. Rudy et al.[19–21] used graphite furnaces with induction heating (Pirani-furnace[19]) to measure melting points of refractory materials up to ∼4000 K. While graphite-based furnaces have become ubiquitous with high-temperature materials characterization, there are thermodynamic material constraints that can limit the maximum temperature during experiments. For example, ZrB_2, a commonly studied ultra-high temperature material, forms a eutectic with carbon (graphite) at 2663 K[21]. This eutectic leads to the formation of a liquid phase that interferes with the measurement and can damage graphite crucibles and graphite furnaces. This leaves the upper temperature for material study to be limited well below the measured melting point of ZrB_2 (3323 K [22]). While the Pirani-furnace used by Rudy et al.[19–21] in the 1960s–1970s was able to measure the melting point of materials like HfB_2 (Tm = 3653 K[22]) and HfC (Tm = 4173 K[20]), it was not able to probe these materials in the liquid state itself. This led to the development of high-temperature containerless methods that avoid all sample contact (and thus contamination) from the container, overcoming the inherent challenge with conventional graphite furnaces. These containerless methods also allow for materials diagnostics on high-temperature liquid phases.

High-temperature containerless methods have been widely used to study materials and include techniques like (1) electromagnetic levitation (EML),[23,24] (2) electrostatic levitation (ESL),[25–29] (3) acoustic levitation,[30–33] and (4) aerodynamic levitation.[34–36] In addition to avoiding chemical contamination, the use of these containerless sample environments avoids extrinsic heterogenous nucleation of crystals. This enables supercooling of liquids often by several hundreds of degrees below their equilibrium melting points. These systems have been used to measure thermal expansion,[37–39] phase transformations,[37,38,40] creep,[41,42] melting points,[43–45] surface tension,[33,46–50] and viscosities[32,45–49] at high temperatures. The systems that are currently in operation have been optimized for either oxide or metallic materials, and the highest reported temperatures are ∼3773 K[51] on oxide systems in oxygen using aerodynamic levitation and ∼3673 K on non-oxide systems in inert atmospheres[41,52] using ESL. More information on levitation techniques can be found in the following reviews.[53–56]

The environmental controlled conical nozzle levitator (E-CNL) equipped with dual-wavelength lasers (CO_2 and Yb) is an aerodynamic levitation system designed in collaboration with Materials Development Inc. (MDI) to study ultra-high temperature materials and UHTCs (both oxide and non-oxide) in a controlled (varying gas composition), containerless environment, up to and beyond ∼4000 K. The E-CNL addresses the two key problems with studying UHTCs. Many UHTCs and ultra-high-temperature materials of interest can have a range of electrical conductivity at various temperatures. Poor electrical conductivity at low temperatures precludes effective use of radio frequency heating. Directed energy (laser) beam heating is an attractive solution because it can provide localized deposition of energy. However, insulators typically absorb well in the mid-infrared range (e.g., CO_2 laser, 10.06 μm) while more metallic materials reflect these wavelengths. Conversely, shorter infrared wavelengths (e.g., Yb-fiber laser 1.06 μm) are absorbed well by conductive materials but poorly by insulators. By combining both of these lasers in a way that allows controlled application of two wavelengths, many of the heating issues that cannot be addressed by simply using a single higher-powered laser can be avoided. The use of aerodynamic levitation provides containerless heating and completely avoids contact with other materials. As shown in prior work, this approach avoids contamination due to container interactions.

This article describes the E-CNL system and a series of key characterization experiments to verify the system's capabilities. The following sections demonstrate that the E-CNL has: (1) successfully measured the melting points of refractory oxides (insulator, high emissivity materials) and refractory non-oxides (conductive, low emissivity materials) to within 0.17–2.43 % of reported literature values, showing high-temperature accuracy, (2) successfully achieved a maximum operating temperature of ~4250 ± 34 K, measured using a specially made high-temperature pyro pyrometer (Pyrofiber II—Pyrometer LLC) on a molten 76.6 mg HfO_2 sample with a normal spectral emissivity (NSE) of 0.91 (λ = 0.65 μm),[57] and (3) successfully controlled the levitation gas environment (oxygen to argon) at temperatures upwards of 3173 K on either solid or molten samples while maintaining a relatively stable temperature. These capabilities will enable a series of novel high-temperature experiments within the E-CNL system up to 4000 K, such as (1) high-temperature diffusion experiments and (2) high-temperature solid-gas reactions (oxidation experiments), which will be essential for next generation high-temperature-integrated material systems.

This is a novel testing apparatus using proven methods for high temperature measurements. The combined use of levitation, atmospheric controls, dual laser heating, and dual pyrometers enables measurements of a variety of materials to high temperatures in a precisely controlled atmosphere. These capabilities demonstrated in the E-CNL system will be essential for the characterization of the ultra-high temperature materials which will be necessary for future galactic travel and energy generation here on Earth.

1.1 | E-CNL equipped with dual-wavelength lasers instrument design

The E-CNL system is equipped with dual 400 W CO_2 (10.6 μm; Synrad) and 500 W Yb (1.07 μm) (IPG Photonics) lasers (Figure 1). This system utilizes an IR-CAS8CS 0.9 μm pyrometer (1000–3800 K, specified instrument error [0.5% error below 1773 K, 1% error between 1773 and 2273 K, 2% error above 2273 K],[58] 100 Hz, 190 mm working distance; Chino Corporation) and a high temperature Pyrofiber II 0.65 μm pyrometer (2800 – 5000 K, specified instrument error [±3 K],[59] 35 Hz, 200 mm working distance) (Pyrometer LLC) for noncontact measurement of sample surface temperature. These pyrometers were selected to operate at wavelengths (0.9 and 0.65 μm) that would minimize interference with the CO_2 (10.6 μm) and Yb fiber (1.07 μm) lasers while maintaining measurement accuracy. The sample can be observed using a KP-D20AU camera (Hitachi Kokusai Electric America) equipped with a TG10Z0513FCS auto-iris lens (Computer CBC America). Sample levitation is achieved using a conical nozzle where inlet gas flow is controlled by two 2000 SCCM GE50A013203SBV020 gas flow controllers (MKS Instruments Inc.). The gas flow controllers, pyrometers, and lasers are integrated and controlled via a custom LabVIEW (National Instruments) software program developed by MDI. For oxygen-sensitive samples, the chamber is connected to a roughing pump vacuum system, capable of achieving a vacuum of ~0.005 atm, to remove residual air. The chamber can then be backfilled with ultra-high purity argon passed through a MC-1-902 room-temperature catalytic getter (Entegris) specified to achieve a partial pressure of oxygen as low as 10^{-9} atm (1 ppb). This chamber is also equipped with a pressure relief system and rapid chamber filling valve. Thus, refractory metals, carbides, and borides can be formed into beads[60,61] and levitated[43] in an inert gas stream, preventing sample-container reactions.

The ideal samples for levitation are ~2–3 mm diameter spheroids. These samples can be fabricated via a variety of forming techniques: (1) laser hearth melting,[62] (2) vibrating table,[60,61] (3) gel casting,[39] and (4) machining. The hearth melting method involves heating powdered samples in a copper hearth using a laser, which forms a sphere from the melts surface tension.[62] The vibrating table method involves forming a slurry using powder, a binder (methyl cellulose), a dispersant (Ammonium Polymethacrylate Darvan C-N), and a solvent (water) and placing this slurry on a vibrating table with enclosed walls at ~70 Hz.[60,61] This causes the slurry to bounce and deform, thereby forming a spherical shape that requires drying and calcination. Gel casting involves forming a slurry with powder, a polymer, a cross-linking agent, and water which is drop-cast into a hot silicone oil with a surfactant. These samples are then calcined.[39] The machining method typically involves grinding or turning a rod or preform to make a spherical sample. The samples used in this study were commercially purchased or synthesized via the vibrating table method using 90 kD (Hydroxypropyl)methyl cellulose (Sigma-Aldrich) and Ammonium Polymethacrylate solution Darvan C-N (Vanderbilt Minerals, LLC). Key flow characteristics of aerodynamic levitation were analyzed by Nordine and Atkins.[63] For more details regarding these processing conditions, please refer to references: [39,60–63]. Ceramic solid oblate spheroids at ~3200 K can have temperature gradients up to ~500 K/mm (depending on processing), which can be reduced to ~15 K/mm if the sample is a perfect dense sphere that rotates on all axes, distributing the heat over the materials surface. When molten, this temperature gradient can be reduced to ~5 K/mm through forced convection.[61] Porous samples can

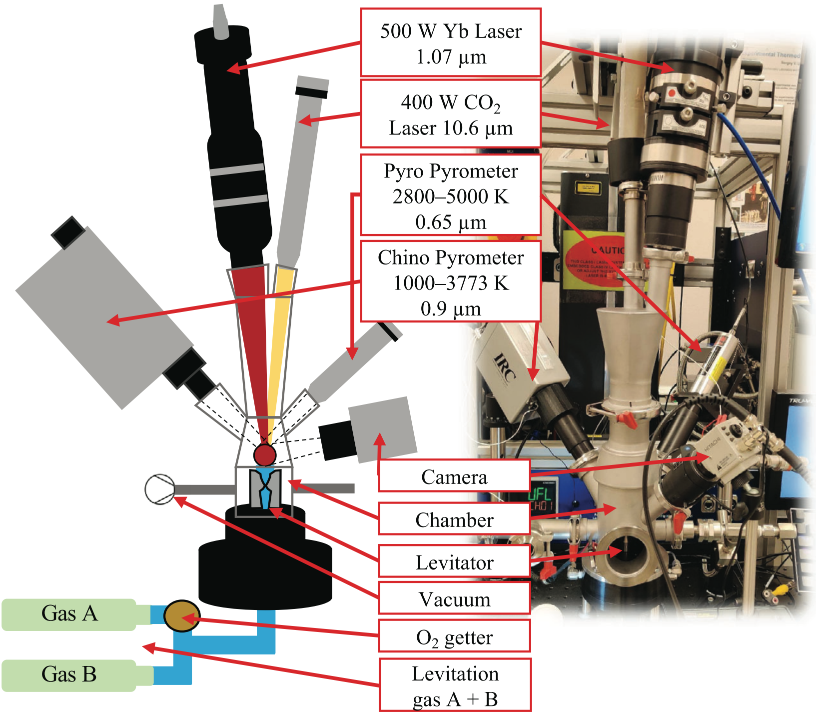

FIGURE 1 Schematic and photo of the environmentally controlled levitation (E-CNL) system equipped with dual wavelength 400 W CO_2 (10.6 μm) and 500 W Yb (1.07 μm) lasers.

be levitated and melted; however, porous samples exhibit higher temperature gradients in the solid state compared with dense samples.

1.2 | Demonstration of E-CNL capabilities

The E-CNL system was designed to study ultra-high temperature materials: refractory metals, carbides, and borides at high temperatures. To validate the high temperature capabilities of the system, a series of high temperature experiments were conducted as discussed below. These include: (1) high-temperature melting point experiments to verify accuracy in temperature measurements, (2) high temperature dual wavelength laser experiments to verify the maximum temperature achieved in the system, and (3) environmental control experiments to verify levitation gas control while maintaining temperature. In these experiments, a sample is loaded onto the nozzle, and if necessary, the chamber is evacuated using a roughening pump and refilled with gas. The levitation gas is flowed at an appropriate rate to levitate the sample, the pyrometers and lasers are aligned to single point on the sample, then the lasers are turned on and slowly increase in power until the desired temperature is reached.

1.3 | Melting point verification

As with any instrument, standards are required to verify the properties measured. Here, the E-CNL is used to measure the melting point of four oxides and four nonoxides with known high-temperature melting points. These materials are listed, along with their literature-reported melting points and NSE in Table 1.

Under appropriate conditions (e.g., rapid cooling, stably levitating sample), materials brought to a liquid state can remain liquid at temperatures below their melting point temporarily existing in an undercooled state. The temperature of these samples will then rise suddenly as they solidify due to the release of the latent heat of fusion, a phenomenon known as recalescence.[64] In this work, the melting temperature is determined by the recalescence

TABLE 1 Literature melting point compared with measured melting point using room temperature literature normal spectral emissivity (NSE) ($\lambda = 0.9\ \mu m$). Multiple melting points in the literature are tabulated to show the spread in the measurements. The melting point selected for direct comparison was based on the reported impurities and the techniques used in the measurements (Supporting information S2).

Materials	Literature melting points (K) (underlined values used in Figure 2 and to calculate accuracy)	Measured melting point (K) (mean ± standard deviation [pyrometer error] [n = trials])	Accuracy (comparison to the underlined literature value) (%)	Literature NSE ($\lambda = 0.9\ \mu m$)
TiO_2	2143 ± 15[71] 2113 ± 10[72]	2091 ± 3 (18) [n = 9]	−2.43	0.87* [73]
Al_2O_3	2327 ± 6[74] 2327 ± 6[75] 2344 ± 20[76]	2310 ± 3 (46) [n = 10]	−0.73	0.93[77,78]
ZrO_2	2973 ± 30[79] 2979 ± 20[57] 2963 ± 30[80]	2984 ± 31 (59) [n = 6]	0.37	0.87**[81]
HfO_2	3123 ± 20[82] 3173 ± 30[80] 3073 ± 30[79] 3076 ± 15[74]	3199 ± 45 (64) [n = 5]	2.43	0.69[83]
Ni	1728 ± 3[84] 1726[85]	1740 ± 10 (7) [n = 6]	0.69	0.31[86,87]
Ti	1943 ± 5[88] 1941 ± 10[89] 1933[90] 1923[91]	1983 ± 16 (16) [n = 6]	2.06	0.39[92,93]
Nb	2750 ± 10[94] 2740 ± 20[95] 2749[96] 2741[97]	2701 ± 12 (54) [n = 4]	−1.78	0.31***[98,99]
Ta	3290 ± 20[95] 3269 ± 7[100]	3368 ± 24 (67) [n = 7]	2.37	0.19[101]

*NSE at 2250 K.

**NSE at 2273 K.

***NSE at 1000 K.

peak observed through cooling trace experiments.[30,65] This involves using the CO_2 and Yb lasers to heat the spherical levitating samples until they are completely molten while the Chino pyrometer (0.9 µm) measures the surface temperature. Due to the absorbance of the samples, the CO_2 laser was primarily used to heat oxides (insulators), and the Yb fiber laser was primarily used for the non-oxide (conductors) samples. When the CO_2 and Yb fiber lasers are turned off, the levitating sample cools rapidly, undergoing recalescence. The recalescence is observed as a heat effect in the thermogram as represented in Figure 2 where the arrest in cooling is a result of a phase change from liquid to solid.

To accurately determine the surface temperature of samples used in this study, two corrections are applied to the pyrometer measurements: (1) system corrections that account for pyrometer lens, observation angles, and working distances and (2) material-specific corrections such as the material's emissivity.

System corrections involve using the Lambert-cosine rule (Equation (1)) and Fresnel equation (Equation (2)). Since the working distance of the pyrometer was sufficiently large (190 mm), the effect of the angle as exhibited by the Lambert-cosine rule (Equation (1)) was negligible and could be ignored allowing the use of NSE values for correction. Further corrections were applied to account for

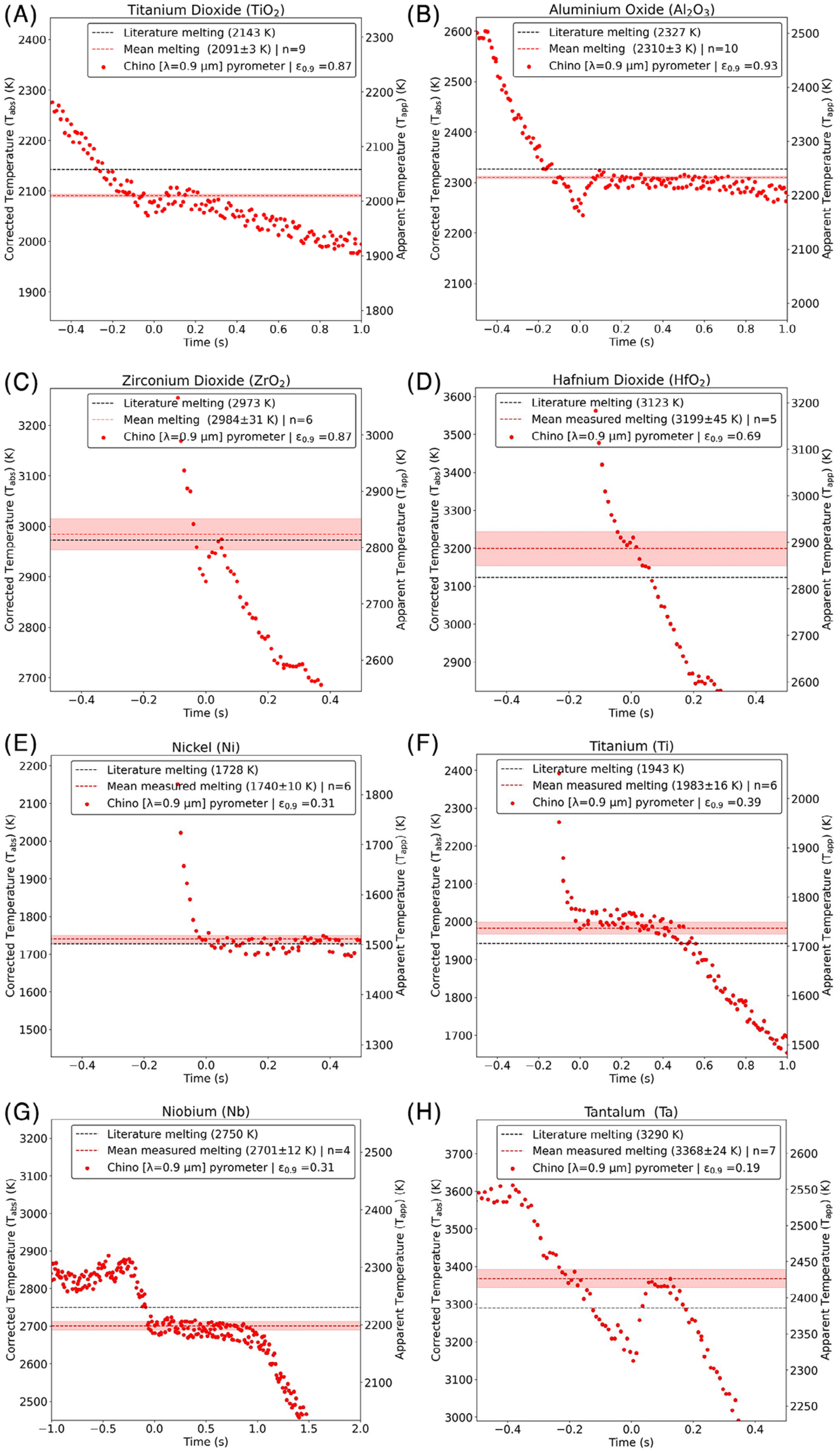

FIGURE 2 Representative cooling traces of oxides (TiO_2, Al_2O_3, ZrO_2, and HfO_2) and non-oxide materials (Ni, Ti, Nb, and Ta) collected using the E-CNL system. The melting point is determined by the recalescence observed during cooling from the melt. The time along the *x*-axis was set to zero at the start of recalescence, which was defined as the first positive change in slope. The red dashed line represents the mean melting point, and the red shaded area represents one standard deviation of *n* trials. The black dashed line is the value reported in the literature (Table 1). The apparent temperature (T_{app}) is the pyrometer reading. This is corrected using Equations (1)–(3), using the NSE from the literature (Table. 1). The data for all materials and their trials are provided in the Supporting information (S2).

emitted light from the sample passing through each glass surface (Equation (2)). The light emitted from the sample passes through two BK7 optical glass windows for a total of four surfaces before reaching the pyrometer detector.[66] Using Equation (2) the reflectivity for each surface at 0.9 μm is approximately 4%. This results in an effective transmission of 85%. This value is applied in Equation (3) as a coefficient to the NSE.

$$\varepsilon_{\mathrm{NSE}} = \varepsilon_{\lambda} \cos\theta. \tag{1}$$

Equation 1: Lambert-cosine rule where $\varepsilon_{\mathrm{NSE}}$ is the corrected NSE, ε_{λ} is the angular spectral emissivity, and θ is the observation angle to the surface normal.[67]

$$R_{\lambda} = \frac{(n_{\lambda} - 1)^2 + {k_{\lambda}}^2}{(n_{\lambda} + 1)^2 + {k_{\lambda}}^2}. \tag{2}$$

Equation 2: Fresnel equation used to determine temperature correction for chamber and pyrometer windows. R_{λ} is the reflectivity for a given wavelength. $n_{\lambda}$is the index of refraction for the given surface at the given wavelength. $k_{\lambda}$is the extinction coefficient for a given material at a given wavelength. The extinction coefficient is often negligible for sufficiently thin windows. More information can be found in the Supportng information (S1).

The value measured by the pyrometer (apparent temperature—T_{app}) is corrected based on the instrument corrections (discussed above) and the sample's emissivity. The correction is done using the modified Wein's approximation to Planks law as shown in Equation (3). In order to use Equation (3) to correct the apparent temperature, the emissivity must be determined at the pyrometers specified wavelength. Full calculations for temperature correction can be found in the Supporting information (S1).

$$\frac{1}{T_{\mathrm{abs}}} = \frac{1}{T_{\mathrm{app}}} + \frac{\lambda \ln \varepsilon}{C_2}. \tag{3}$$

Equation 3: Wien's equation, where T_{abs} and T_{app} are the absolute (corrected) and apparent (as measured) temperature measured in K, λ is the pyrometers operating wavelength in μm (0.9 μm for the Chino pyrometer, 0.65 μm for the Pyro pyrometer), ε is the unitless emissivity at the pyrometer wavelength, and C_2 is the second radiation constant of 14388 μm K.

Commercially manufactured beads of 3 mm aluminum oxide (99.8 %), 3 mm nickel (99.0 %), 3 mm titanium (99.6 %), 4 mm niobium (99.9 %) (Goodfellow), and 2.73 mm tantalum (99.77 %, X-medics) were purchased, while 3 mm titanium dioxide (99.8 %), zirconium dioxide (99.99 %), and hafnium dioxide (98 %) (Sigma-Aldrich) beads were fabricated using the vibrating table method.[60,61]

The oxides (TiO_2, Al_2O_3, ZrO_2, and HfO_2) were levitated in simulated air (80 % Ar/20 % O_2), while the air-sensitive non-oxide (Ni, Ti, Nb, and Ta) materials were levitated in ultra-high purity Ar passed through the oxygen getter. NSE values were chosen from literature at room temperature unless otherwise specified, at the Chino pyrometer's wavelength (0.9 μm). Many factors can affect the emissivity of a sample including surface roughness,[68] measurement angle,[69] presence of oxygen vacancies and impurities,[70] and temperature. The key sample measurement is taken at the melting point upon freezing after being molten and supercooled. For these melting point measurements, the surface roughness is comparable as they all result from quenching from the melt. Table 1 contains the literature NSE used for temperature correction.

For each material, several trials ($4 \le n \le 10$) were analyzed. For each trial the series of data points where the temperature is nearly constant at the melting point after freezing were averaged. This value was taken as the melting point for each trial. The mean of those trials was determined as the measured melting point for each material. The standard deviation between the trials is represented as the light red bands in Figure 2 (±1 standard deviation). To represent the cooling traces for each material a single representative trial was plotted in Figure 2. The data for each trial can be found in the Supplementary information (S2).

The accuracy of a measurement is related to how close a measurement is to the true value, whereas the precision of a measurement is related to the measurement reproducibility. The error in measured temperature when using the Chino pyrometer is 0.5% between 1273 and 1773 K, 1.00% between 1773 and 2273 K, and 2.00 % above 2273 K.[58] When comparing the measured mean melting point values with the literature the accuracy is 0.69–2.45%. This is in the range of error of the Chino pyrometer indicating the measurements are at the limit of the instrument's capability. The standard deviations in measured melting point range from 3–45 K indicating the high precision and reproducibility of the measurements. The form of the recalescence feature is the key factor for the precision of the melting point measurement. The cooling traces demonstrated by TiO_2 (Tm = 2091 ± 3 K) and Al_2O_3 (Tm = 2310 ± 3 K) (Figure 2A, B) have high precision due to the pronounced recalescence feature. Comparably, the cooling traces demonstrated by HfO_2 (Tm = 3199 ± 45 K) and ZrO_2 (Tm = 2984 ± 31 K) (Figure 2C, D) have lower precision with a less pronounced recalescence feature. This observation is independent of the magnitude of the melting point of the material as Ta (Tm = 3368 ± 24 K) and Nb (Tm = 2701 ± 12 K) (Figure 2G, H) demonstrate relatively high precision with pronounced recalescence features. The relatively low standard deviation in measured melting points demonstrates the E-CNL system can successfully measure the melting points of both oxide (insulator) and non-oxide (conductor) materials. This is significant as it demonstrates that when measuring melting points of air-sensitive, non-oxide materials, the partial pressure of oxygen within the system is low enough to not shift the measured melting point values far from literature values. The mean ± standard deviation measured in the experiments are summarized in Table 1.

In situ high-temperature NSE data up to melting at the pyrometer's wavelength is sparse in the literature. Thereby a degree of discrepancy between the emissivity value used for the correction and the true emissivity of the sample can arise. To overcome this, some use multi-wavelength pyrometers (e.g., two-color pyrometers and/or spectropyrometers) for in situ temperature correction. While useful, these systems are still not perfect. This temperature correction assumes that the emissivity is not a function of wavelength (a grey body), an assumption that is not valid for all materials. In multiwavelength pyrometers where many channels (wavelengths) are used, the acquisition time increases. Absorption-corrected pyrometers can also be used. These pyrometers will measure the samples' absorption using a laser to determine the spectral emissivity at the wavelength of the laser in situ. Again, although useful, these systems are not perfect as emissivity has angular dependence and some samples can be partially transparent to the incoming laser's wavelength. Some of the best high-temperature measurement work was completed by Rudy et al.[19–21] in the 1960s–1970s. Rudy[19–21] utilized a Pirani furnace to heat conductive samples to ∼4000 K using joule heating. Temperature was measured by drilling black body cavities into the samples. The black body cavities were designed to exhibit an emissivity approaching 1.00 regardless of material, reducing the emissivity correction problem. However, black body holes can only be used for uniform temperature, solid samples.

To illustrate the relationship between NSE error and its effect on measured temperature error, Equation (3). was used to produce Figure (3). This figure shows how an error in NSE will propagate to an error in temperature. For a selected NSE, absolute (T_{abs}) and apparent (T_{app}) temperatures were calculated. Then, varying NSE values were chosen, and using the same apparent temperature values, absolute values were calculated. The error in absolute temperature determination is then plotted at each temperature for each NSE. Figure 3A is for high NSE materials, like oxides, where the emissivities of TiO_2 (0.87, black line) and HfO_2 (0.69, dashed line) are plotted. Figure 3B is for low NSE materials like metallic materials, where the emissivities of Ta (0.19, black line) and Ti (0.39, dashed line) are plotted. The colored plots represent how the error in temperature will change if there is an error in emissivity. For example, in Figure 3A, the blue solid line represents an NSE of 0.87 minus 25% (=0.6525), while the blue dashed line represents an NSE of 0.69 minus 25% (=0.5175). Note that NSE values >1 are not represented on these plots (this occurs when adding a percentage onto a high NSE number, e.g., 0.87 plus 25%). The difference in the selected NSE is shown by the shaded regions. The size difference in these areas is not related to non-oxide or metallic materials but rather comes from the values of NSE selected to plot (i.e., 0.87 and 0.69 in Figure 3A). A key observation is that the error in NSE diverges as temperature increases, meaning that the same error in NSE will lead to an increase in error in the measured temperature as the temperature of the object increases.

TABLE 2 Literature normal spectral emissivity (NSE) values compared with estimated NSE values based on the mean measured melting point shown in Table 1.

Material	Literature NSE ($\lambda = 0.9$ µm)	Estimated NSE at melting ($\lambda = 0.9$ µm)	Difference in NSE ($\lambda = 0.9$ µm) (%)
TiO_2	0.87*[73]	0.72	−17.24
Al_2O_3	0.93[77,78]	0.88	−5.38
ZrO_2	0.87**[81]	0.89	2.30
HfO_2	0.69[83]	0.78	13.04
Ni	0.31[86,87]	0.33	6.45
Ti	0.39[92,93]	0.46	17.95
Nb	0.31***[98,99]	0.28	−9.68
Ta	0.19[101]	0.21	10.53

*NSE at 2250 K.
**NSE at 2273 K.
***NSE at 1000 K.

If the literature melting point is taken as the reference value, the NSE of the samples being studied can be calculated (estimated) at the melting point, at the pyrometer's wavelength of 0.9 µm. These values along with their percentage difference to room temperature literature values are summarized in Table 2. These values are plotted in Figure 3A, B. The absolute difference in estimated NSE at melting compared with literature NSE is 2.30–17.95%. Materials that were observed to have notably high discrepancies in NSE include Ti (17.95%), HfO_2 (13.04%), and TiO_2 (−17.24%). Also note, that this discrepancy corresponds to a measured melting point difference (when using literature NSE) for Ti (2.06% melting point difference), HfO_2 (2.43% melting point difference), and TiO_2 (−2.43% melting point difference). This result and the analysis in Figure 3 are both helpful and hopeful in highlighting that NSE errors on the order of 17% will only result in melting point errors 2.06–2.43%, whereas the accuracy of the Chino pyrometer is 1–2% at these temperatures. Similar errors in NSE and

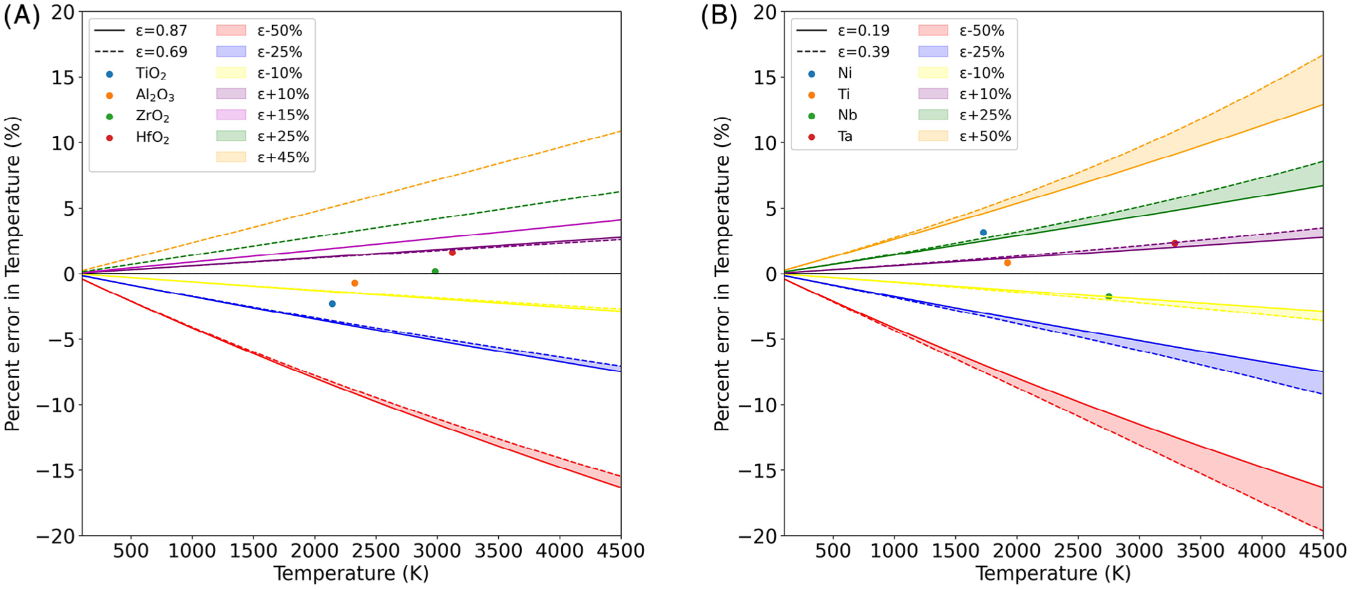

FIGURE 3 The error in temperature is associated with varying degrees of error in normal spectral emissivity (NSE) ($\lambda = 0.9\ \mu m$). (A) shows high NSE (oxide) materials while (B) shows low NSE (non-oxide/metallic) materials. The difference in literature and calculated NSE at the melting point as shown in Table 2 is plotted to highlight the percent error in temperature. Note that NSE values >1 are not represented. These plots were produced using Equation (3). The data points used in this plot can be found in the Supporting information (S3).

temperature measurement as observed with these materials and shown in Figure 3 will likely be observed in other systems depending on the available or obtained emissivity values.

Figure 3 illustrates the degree to which a change in emissivity affects melting temperature measurements made by the E-CNL using this pyrometry technique. More accurate measurements could be made using NSE values at elevated temperatures, but these values are not always available for all materials. Correction for the emissivity of a sample is necessary for pyrometry measurements. Pyrometry is the primary method used for measuring temperatures approaching and above ~2600 K as even high temperature thermocouples tend to degrade due to diffusion across the junction. The purpose of Figure 3 is to show how NSE affects the measured temperature using the correction method in the study. All uncorrected values equivalent to NSE equal to 1 are reported in the supplemental information.

1.4 | Highest temperature observed in the E-CNL system (425 ± 34 K)

When using the E-CNL system to study the highest-temperature materials, it is important to understand the highest achievable temperature. Validating temperature measurements above ~3700 K becomes difficult as the number of materials with reliably measured melting points is very limited. To assess these higher temperatures, a custom Pyrofiber II 0.65 µm (2800–5000 K, specified instrument error [±3 K],[59] 35 Hz, 200 mm working distance; Pyrometer LLC) pyrometer was used, which is calibrated to measure temperature up to 5000 K.

To date, the highest temperature measured using the Pyrofiber II pyrometer was 4250 ± 34 K on a HfO_2 sample NSE 0.91[57] $\lambda = 0.65\ \mu m$. This was achieved by heating the sample using the Yb fiber laser (1.07 µm) at 60% power and the CO_2 laser (10.6 µm) at 50% power. Figure 4 shows the heating and laser power procedure, along with the measured surface temperature. The laser power was increased to heat the sample. Once the sample temperature began to decrease, the lasers were turned off and the experiment concluded. The HfO_2 sample was 76.6 mg at the start of the experiment. At higher temperatures, the sample began rapidly evaporating and was 62.6 mg after the experiment.

While this measurement is significant and highlights that the E-CNL system can achieve exceptionally high temperatures, more work is required. The next series of experiments to be conducted will be to measure the melting points of a series of di-borides: TiB_2 (Tm = ~3193 K[22]) ZrB_2 (Tm = ~3323 K[22]), NbB_2 (Tm = ~3323 K[22]), HfB_2 (Tm = ~3513 K[22]), TaB_2 (Tm = ~3473 K[22], carbides: TiC (Tm = ~3340 K[20]), ZrC (Tm = ~3784 K[102]), NbC (Tm = ~3886 K[20]), HfC (~4201K[20]) TaC (Tm = ~4168 K[20]) and the highest estimated melting point materials $Ta_{0.8}Hf_{0.2}C$ (Tm = ~4178 K[103]) and Hf(C,N) (Tm = ~4135 K[104]). These experiments will be challenging, exciting, and impactful for three key reasons: (1) the melting points of these materials are not well established as there are only

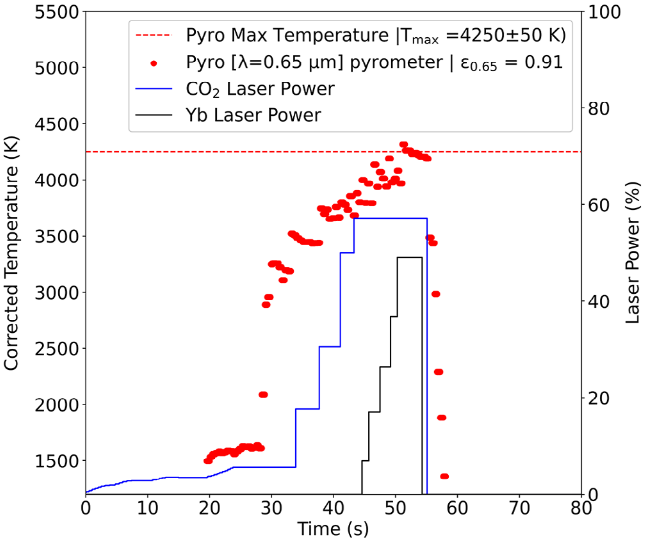

FIGURE 4 The highest temperature achieved by this system, 4250 ± 34 K, on a HfO_2 sample as determined by the Pyrofiber (0.65 μm) pyrometer with NSE 0.91.[57] Heating was achieved using the CO_2 laser (10.6 μm) the Yb fiber laser (1.07 μm) simultaneously. The data for this cooling trace can be found in the Supporting information (S4).

a few measurements in the literature, (2) the emissivity of these materials are not well characterized with evidence that some of these materials exhibit changes in NSE (0.29–0.4 in ZrB_2 $\lambda = 0.655\ \mu$m)[105] at high temperature, and (3) their melting points are all high, with some approaching the upper limit measured on HfO_2 (4250 ± 34 K).

1.5 | Environmental control during experiments

The E-CNL system was designed to study materials in coupled extreme environments: temperatures above ~4000 K and in controlled atmospheres. This will enable high-temperature diffusion experiments well above previously studied temperatures and gas-based reactions such as controlled oxidation in both the solid and liquid phases.

As demonstrated in Figure 5, the E-CNL system can levitate solid and molten samples in changing gas environments at stable temperatures >3000 K. A purchased 3 mm yttria-stabilized-zirconia sample [5 mol% Y_2O_3] (Goodfellow) was levitated at 1000 cc/min total gas flow. The sample was held at a constant temperature in pure O_2, pure Ar, and a variety of changing gas ratios. The rate of changing gases did not dramatically affect the temperature of the sample. To demonstrate this, the gas rate was changed from Ar to O_2 and back to Ar in increments of 1%, 10%, 50%, and 100%. The sample was held at 1745 K (Figure 5A), 2700 K (Figure 5B), and 3175 K (Figure 5C). For the 1745 K hold (Figure 5A), the sample mean temperature was 1745 ± 16 K during the Ar hold, 1742 K ± 22 K during the O_2 hold, and 1744 K ± 22 K during the gas switching. For the 2700 K hold (Figure 5B), the sample mean temperature was 2703 ± 22 K during the Ar hold, 2699 K ± 19 K during the O_2 hold, and 2701 ± 27 K during the gas switching. For the 3175 K hold (Figure 5C), the sample mean temperature was 3174 ± 12 K during the Ar hold, 3175 K ± 16 K during the O_2 hold, and 3179 ± 16 K during the gas switching. The melting temperature of yttria-stabilized zirconia [5 mol% Y_2O_3] is 2973 K[106]; therefore, the sample was molten during the 3175 K hold.

The changing of gas ratios did not significantly affect the temperature or levitation of the sample. This enables experiments where samples can be exposed to changing atmospheres while being heated. The atmosphere can be selected to imitate air for the oxides, and to be inert for the metals. Future experiments will leverage this capability to examine the effects of oxygen on sensitive samples. These studies are expected to use oxygen isotopes (^{18}O) to investigate diffusion in extreme-temperature materials. Heavy oxygen can be introduced at high temperature to oxide samples and allowed to diffuse. Those samples can be characterized ex situ to determine oxygen diffusion profiles and thus oxygen diffusion coefficients at high temperatures. Further experiments could introduce oxygen to oxygen-sensitive samples to observe high-temperature oxidation. Future in situ emissivity measurements will be key to determining the temperature as the composition of the sample changes.

2 | CONCLUSION

The E-CNL system has successfully measured the melting point of several oxide materials (TiO_2, Tm = 2091 ± 3 K; Al_2O_3, Tm = 2310 ± 3 K; ZrO_2, Tm = 2984 ± 31 K; and HfO_2, Tm = 3199 ± 45 K) and several air-sensitive refractory metals (Ni, Tm = 1740 ± 10 K; Ti, Tm = 1983 ± 16 K; Nb, Tm = 2701 ± 12 K; and Ta, Tm = 3368 ± 24 K—note: mean ± standard deviation) during levitation which matched literature values within 0.69–2.43%, demonstrating high accuracy and precision at high temperature. This containerless measurement approach is critical for probing properties without container-contamination and the dual wavelength laser heating is essential to heat both poor electrical conductors (refractory metals and carbides) and insulators (oxides).

The highest temperature achieved in the system was ~4250 ± 34 K using an NSE of 0.91[57] to characterize a molten 76.6 mg HfO_2 sample.

Stable levitation was demonstrated on spherical samples (yttria-stabilized zirconia) while adjusting the levitation gas composition from pure oxygen to pure argon, verifying atmospheric control up to 3173 K on either solid or molten samples.

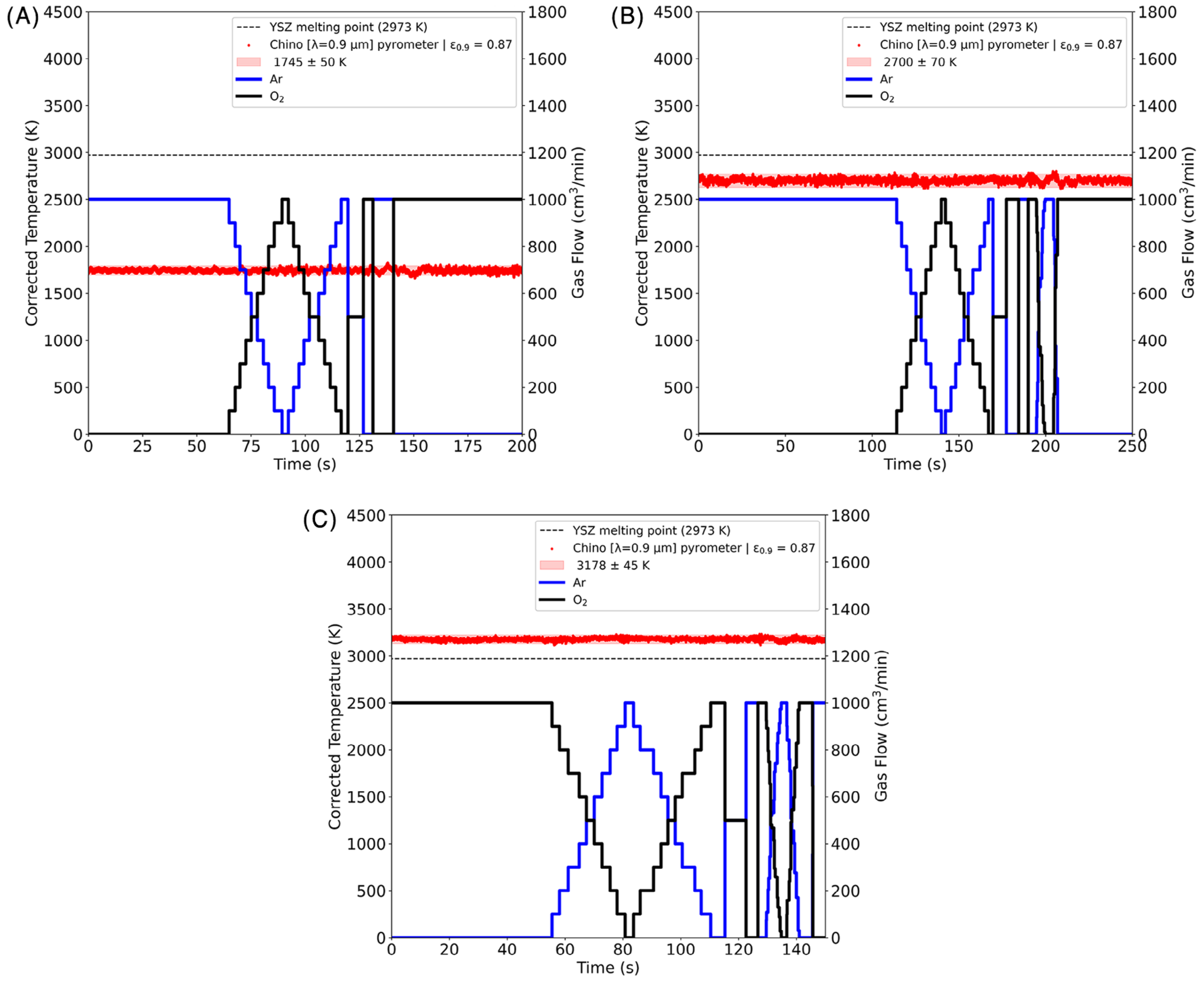

FIGURE 5 Controlled environment experiments performed on a YSZ (5 mol% Y_2O_3) sample demonstrates the ability to maintain a consistent temperature of the sample while varying the ratios of the levitation gas. The sample is held at 1745, 2700, and 3175 K in argon, oxygen, and a combination of both gases. The data used for each of these plots can be found in the Supporting information (S5).

These successes demonstrate the viability of in situ high-temperature environmentally controlled studies potentially up to 4000 K for (1) high temperature diffusion experiments and (2) high temperature solid-gas reactions (oxidation experiments), both of which will be essential for next-generation high temperature integrated material systems. Material property measurements demonstrated using the E-CNL will be essential for the development of next generation materials for hypersonic platforms, nuclear fission and fusion, and space exploration.

ACKNOWLEDGEMENTS

This work was funded by the National Science Foundation (NSF) in the Directorate for Mathematical and Physical Sciences (MPS), under the Division of Materials Research (DMR), in the Ceramic (CER) program. Award number: 2047084.

CONFLICT OF INTEREST

The authors declare no conflict of interest.

ORCID

Scott J. McCormack https://orcid.org/0000-0002-0715-3451

REFERENCES

1. Wuchina E, Opila EJ, Opeka M, Fahrenholtz WG, Talmy IG. UHTCs: Ultra-high temperature ceramic materials for extreme environment applications. Electrochem soc. Interface. 2007;16.
2. Lynam A, Romero AR, Xu F, Wellman RW, Hussain T. Thermal spraying of ultra-high temperature ceramics: a review on processing routes and performance. J Therm Spray Tech. 2022;31:745–79.
3. Mars 2020 Perseverance Landing Press Kit | Getting to Mars. https://www.jpl.nasa.gov/news/press_kits/mars_2020/landing/mission/spacecraft/getting_to_mars/

4. Jaworski W, Nagler RG. A parametric analysis of Venus entry heat- shield requirements. 1970. Preprint at: https://ntrs.nasa.gov/citations/19700018760
5. *The Atmospheric Reentry Demonstrator*. 1998. https://www.esa.int/esapub/br/br138/br138.pdf
6. Space Nuclear Propulsion for Human Mars Exploration. National Academies Press, 2021. doi:10.17226/25977
7. Memorandum on the National Strategy for Space Nuclear Power and Propulsion (Space Policy Directive-6)—The White House. 2021. https://trumpwhitehouse.archives.gov/presidential-actions/memorandum-national-strategy-space-nuclear-power-propulsion-space-policy-directive-6/
8. Trip to Mars—NASA Mars. https://mars.nasa.gov/mars2020/timeline/cruise/#
9. Hall L. New Class of Bimodal NTP/NEP. 2023.
10. Chapin D, Kiffer S, Nestell J. *The Very High Temperature Reactor: A Technical Summary*. 2004. http://large.stanford.edu/courses/2013/ph241/kallman1/docs/chapin.pdf
11. *Fact Sheet: Developing a Bold Vision for Commercial Fusion Energy | The White House*. 2022. https://www.whitehouse.gov/ostp/news-updates/2022/03/15/fact-sheet-developing-a-bold-vision-for-commercial-fusion-energy/
12. Fahrenholtz WG, Hilmas GE. Ultra-high temperature ceramics: materials for extreme environments. Scr Mater. 2017;129:94–99.
13. Neuman EW, Hilmas GE, Fahrenholtz WG. Strength of zirconium diboride to 2300°C. J Am Ceram Soc. 2013;96:47–50.
14. Neuman EW, Hilmas GE, Fahrenholtz WG. Ultra-high temperature mechanical properties of a zirconium diboride-zirconium carbide ceramic. J Am Ceram Soc. 2016;99:597–603.
15. Feng L, Chen W, Fahrenholtz WG, Hilmas GE. Strength of single-phase high-entropy carbide ceramics up to 2300°C. J Am Ceram Soc. 2021;104:419–27.
16. Neuman E, Brown-Shaklee HJ, Watts JL, Hilmas GE, Fahrenholtz WG. Case study: building an ultra-high temperature mechanical testing system. Am Ceram Soc Bull. 2013;36–38.
17. Touloukian YS, Kirby RK, Taylor ER, Lee TYR. Thermophysical Properties of Matter—the TPRC Data Series. Thermal Expansion—Nonmetallic Solids. 1977;13. Preprint at: https://apps.dtic.mil/sti/citations/ADA129116
18. Touloukian YS, Kirby RK, Taylor RE, Desai PD. Thermophysical Properties of Matter—the TPRC Data Series. Thermal Expansion Metallic Elements and Alloys. 1975;12. Preprint at: https://apps.dtic.mil/sti/citations/ADA129115
19. Rudy E, Pbogulski G. Ternary phase equilibria in transition metal-boron-carbon-silicon systems Part III: Special experimental techniques Volume II: A pirani-furnace for the precision determination of the melting temperature of refractory metallic substances. 1967.
20. Rudy E. *Ternary Phase Equilibria in Transition Metal-Boron-Carbon-Silicon Systems Part V. Compendium of Phase Diagram Data*. 1969.
21. Rudy E, Windisch S. Ternary phase equilibria in transition metal-boron-carbon-silicon systems, Part II. Ternary Systems, Volume XIII. Phase diagrams of the Systems Ti-B-C, Zr-B-C and Hf-B-C. 1968.
22. Post B, Glaser FW, Moskowitz D. Transition metal diborides. Acta Metall. 1954;2:20–25.
23. Bojarevics V, Pericleous K. Modelling electromagnetically levitated liquid droplet oscillations. ISIJ Int. 2003;43:890–98.
24. Etay J, Schetelat P, Bardet B, Priede J, Bojarevics V, Pericleous K. Modelling of electromagnetic levitation—consequences on non-contact physical properties measurements. High Temp Mater Processes (London). 2008;27:439–48.
25. Rhim W Chung SK, Barber D, Man KF, Gutt G, Rulison A, Spjut RE, et al. An electrostatic levitator for high-temperature containerless materials processing in 1-g. Rev Sci Instrum. 1993;64:2961–70.
26. Rhim W-K, Ohsaka K, Paradis P-F, Spjut RE. Noncontact technique for measuring surface tension and viscosity of molten materials using high temperature electrostatic levitation. Rev Sci Instrum. 1999;70:2796–801.
27. Paradis P-F, Ishikawa T. Surface tension and viscosity measurements of liquid and undercooled alumina by containerless techniques. Jpn J Appl Phys. 2005;44:5082–85.
28. Paradis P-F, Ishikawa T, Saita Y. Yoda S. Non-contact thermophysical property measurements of liquid and undercooled alumina. Jpn J Appl Phys. 2004;43:1496–500.
29. Tamaru H, Koyama C, Saruwatari H, Nakamura Y, Ishikawa T, Takada T, et al. Status of the electrostatic levitation furnace (ELF) in the ISS-KIBO. Microgravity Sci Technol. 2018;30:643–51.
30. Weber JKR, Hampton DS, Merkley DR, Rey CA, Zatarski MM, Nordine PC, et al. Aero-acoustic levitation: a method for containerless liquid-phase processing at high temperatures. Rev Sci Instrum. 1994;65:456–65.
31. Nordine PC, Merkley D, Sickel J, Finkelman S, Telle R, Kaiser A. A levitation instrument for containerless study of molten materials. Rev Sci Instrum. 2012;83:125107.
32. Trinh EH, Marston PL, Robey JL. Acoustic measurement of the surface tension of levitated drops. J Colloid Interface Sci. 1988;124:95–103.
33. Bayazitoglu Y, Mitchell GF. Experiments in acoustic levitation—surface tension measurements of deformed droplets. J Thermophys Heat Trans. 1995;9:694–701.
34. Glorieux B, Millot F, Rifflet J-C, Coutures J-P. Density of superheated and undercooled liquid alumina by a contactless method. Int J Thermophys. 1999;20:1085–94.
35. Benmore CJ, Weber JKR. Aerodynamic levitation, supercooled liquids and glass formation. Adv Phys X. 2017;2:717–36.
36. Langstaff D, Gunn M, Greaves GN, Marsing A, Kargl F. Aerodynamic levitator furnace for measuring thermophysical properties of refractory liquids. Rev Sci Instrum. 2013;84:124901.
37. McCormack SJ, Wheeler WA, Hulbert BS, Kriven WM. Directions of zero thermal expansion and the peritectic transformation in HfTiO4. Acta Mater. 2020;200:187–99.
38. McCormack SJ, Weber RJ, Kriven WM. In-situ investigation of Hf6Ta2O17 anisotropic thermal expansion and topotactic, peritectic transformation. Acta Mater. 2018;161:127–137.
39. Converse E. In-situ high temperature spatially resolved X-ray diffraction of TiB2 up to ~3050˚C. J Eur Ceram Soc. 2023,
40. Tobase T, Yoshiasa A, Arima H, Sugiyama K, Ohtaka O, Nakatani T, et al. Pre-transitional behavior in tetragonal to cubic phase transition in HfO_2 revealed by high temperature diffraction experiments. Phys Status Solidi. 2018;255:1800090.

41. Hyers RW, Canepari S. *Advances in Non-contact Measurement of Creep Properties*. 2009. https://ntrs.nasa.gov/api/citations/20090028680/downloads/20090028680.pdf
42. Lee J, Wall JJ, Rogers JR, Rathz TJ, Choo H, Liaw PK, et al. Non-contact measurements of creep properties of niobium at 1985°C. Meas Sci Technol. 2015;26:015901.
43. McCormack SJ, Tseng K, Weber RJK, Kapush D, Ushakov SV, Navrotsky A, et al. In-situ determination of the HfO_2-Ta_2O_5-temperature phase diagram up to 3000°C. J Am Ceram Soc. 2019;102:(8):4848–61. doi:10.1111/jace.16271
44. Price DL, David L. High-temperature levitated materials. Cambridge University Press, 2010.
45. Agca C, Neuefeind JC, McMurray JW, Weber R, Navrotsky A. Melting temperature measurement of refractory oxide ceramics as a function of oxygen fugacity using containerless methods. J Am Ceram Soc. 2020;103:4867–75.
46. Ishikawa T, Paradis P-F, Okada JT, Watanabe Y. Viscosity measurements of molten refractory metals using an electrostatic levitator. Meas Sci Technol. 2012;23:025305 .
47. Ishikawa T, Paradis P-F, Itami T. Yoda S. Non-contact thermophysical property measurements of refractory metals using an electrostatic levitator. Meas Sci Technol. 2005;16:443–51.
48. Hakamada S, Nakamura A, Watanabe M, Kargl F. Surface oscillation phenomena of aerodynamically levitated molten Al_2O_3. Int. J. Microgravity Sci. Appl. 2017;34:340403.
49. Kondo T, Muta H, Kurosaki K, Kargl F, Yamaji A, Furuya M, et al. Density and viscosity of liquid ZrO2 measured by aerodynamic levitation technique. Heliyon. 2019;5:e02049.
50. Siafakas D, *et al.* Measurment of viscosity of SiO2-CaO-Al_2O_3 slag in wide temperature range by aerodynamic levitation and rotating bob mehtods and sources of systematic error. Int. J. Microgravity Sic. Appl. 2018;35:350204.
51. Weber JKR, Tamalonis A, Benmore CJ, Alderman OLG, Sendelbach S, Hebden A, et al. Aerodynamic levitator for in situ x-ray structure measurements on high temperature and molten nuclear fuel materials. Rev Sci Instrum. 2016;87:073902.
52. SanSoucie MP, Vermilion DJ, Rogers JR. The NASA MSFC electrostatic levitation (ESL) laboratory: summary of capabilities, recent upgrades, and future work. 2015. Preprint at: https://ntrs.nasa.gov/citations/20150022349
53. Schreiber DK, Schwaiger R, Heilmaier M, McCormack SJ. Materials properties characterization in the most extreme environments. MRS Bull. 2022;47:1128–42.
54. Hong Q-J, Ushakov SV, Lilova K, Navrotsky A, McCormack SJ. Structure and thermodynamics of oxides/carbides/nitrides/borides at high temperature. Am Ceram Soc Bull. 2023;102:28–35.
55. Nordine PC, Weber JKR, Abadie JG. Properties of high-temperature melts using levitation. Pure Appl Chem. 2000;72:2127–36.
56. Ishikawa T, Paradis P-F. Challenges of handling, processing, and studying liquid and supercooled materials at temperatures above 3000 K with Electrostatic Levitation. Crystals (Basel). 2017;7:309.
57. Noguchi T, Kozuka T. Temperature and emissivity measurement at 0.65 μ with a solar furnace. Sol Energy. 1966;10:125–31.
58. IR-CA Series Radiation Thermometers—CHINO Corporation. https://www.chino.co.jp/english/products/thermometers/ir-ca/
59. Pyrofiber II—Pyrometer. https://www.pyrometer.com/product/pyrofiber-ii/
60. Santos CJE, Nelson AZ, Mendoza E, Ewoldt RH & Kriven WM. Design and fabrication of ceramic beads by the vibration method. J Eur Ceram Soc. 2015;35:3587–94.
61. McCormack SJ, Tamalonis A, Weber RJK, Kriven WM. Temperature gradients for thermophysical and thermochemical property measurements to 3000°C for an aerodynamically levitated spheroid. Rev Sci Instrum. 2019;90:015109.
62. Krishnan S, Felten JJ, Rix JE, Weber JKR, Nordine PC, Beno MA, et al. Levitation apparatus for structural studies of high temperature liquids using synchrotron radiation. Rev Sci Instrum. 1997;68:3512–18.
63. Nordine PC, Atkins RM. Aerodynamic levitation of laser-heated solids in gas jets. Rev Sci Instrum. 1982;53:1456–64.
64. Xu J, Yang T, Li Z, Wang X, Xiao Y, Jian Z. The recalescence rate of cooling curve for undercooled solidification. Sci Rep. 2020;10:1380.
65. Winborne DA, Nordine PC, Rosner DE, Marley NF. Aerodynamic levitation technique for containerless high temperature studies on liquid and solid samples. Metall Trans B. 1976;7:711–13.
66. *Schott. Optical Glass Data Sheets*. https://refractiveindex.info/download/data/2017/schott_2017-01-20.pdf
67. Weik MH. Lambert's cosine law. Computer Science and Communications Dictionary, Springer US Imprint, Boston, MA, 2001. https://doi.org/10.1007/1-4020-0613-6_9901
68. Sabuga W, Todtenhaupt R. Effect of roughness on the emissivity of the precious metals silver, gold, palladium, platinum, rhodium, and iridium. High Temperatures-High Pressures. 2001;33:261–69.
69. Nicodemus FE. Directional reflectance and emissivity of an opaque surface. Appl Opt. 1965;4:767.
70. Zhou Q, Zhu S, Ma Z, Liu Y, Liu L, Gao L. Experimental and first-principles study on the effect of oxygen vacancy on infrared emissivity of CeO_2. Ceram Int. 2022;48:11313–19.
71. Brauer G, Littke W. Über den schmelzpunkt und die thermische Dissoziation von Titandioxyd. J Inorg Nucl Chem. 1960;16:67–76.
72. Pouget P. A Note on the Melting Point of Titanium Dioxide. J Am Ceram Soc. 1952;35:188–188.
73. Alderman OLG, Skinner LB, Benmore CJ, Tamalonis A, Weber JKR. Structure of molten titanium dioxide. Phys Rev B Condens Matter Mater Phys. 2014;90:1–13.
74. Yamada T, Yoshimura M, Somiya S. Redetermination of the solidification points of Al_2O_3, Y_2O_3, and HfO_2 by digital pyrometry with an arc-imaging furnace. High Temp High Press. 1986;18:377–88.
75. Schneider SJ. Cooperative determination of the melting point of alumina. Pure Appl Chem. 1970;21:115–22.
76. Mizuno M, Yamada T, Noguchi T. Phase diagram of the system Al2O3-Nd2O3 at high temperatures. Journal of the Ceramic Association, Japan. 1977;85:90–95.
77. Petrov VA, Vorobyev AY. Spectral emissivity and radiance temperature plateau of self-supporting Al_2O_3 melt at rapid solidification. High Temp High Press. 2003;35:677–89.
78. Krishnan S, Weber JKR, Schiffman RA, Nordine PC, Reed RA. Refractive index of liquid aluminum oxide at 0.6328 μm. J Am Ceram Soc. 1991;74:881–83.

79. Shevthenko AV, Lopato LM. DTA method applikation to the highest refractory oxide systems investigation. Thermochim Acta. 1985;93:537–40.
80. Ruh R, Garrett HJ, Domagala RF, Tallan NM. The Svstern Zirconia-Hafnia. J Am Ceram Soc. 1968;51:23–28.
81. Avdoshenko SM, Strachan A. High-temperature emissivity of silica, zirconia and samaria from ab initio simulations: Role of defects and disorder. Model Simul Mat Sci Eng. 2014;22(7):075004.
82. Coutures JP, Coutures J. The system HfO_2-TiO_2. J Am Ceram Soc. 1987;70:383–87.
83. Liu F, Cheng X, Mao J, Li Q, Zeng X. Effects of rare-earth oxide doping on the thermal radiation performance of HfO_2 coating. Ceram Int. 2019;45:13004–10.
84. Jordan L, Swanger W. The properties of pure nickel. Bureau Stand J Res. 1930;5:1292–306. http://dx.doi.org/10.6028/jres.005.075
85. Adriano DC. Nickel. In: *Trace Elements in Terrestrial Environments*, 677-705. Springer New York, NY 2001. https://doi.org/10.1007/978-0-387-21510-5
86. Price DJ. The emissivity of hot metals in the infra-red. Proc Phys Soc. 1947;59:118–31.
87. Teodorescu G, Jones PD, Overfelt RA, Guo B. Normal emissivity of high-purity nickel at temperatures between 1440 and 1605 K. J Phys Chem Solids. 2008;69:133–38.
88. Ishikawa T, Koyama C, Nakata Y, Watanabe Y, Paradis P-F. Spectral emissivity and constant pressure heat capacity of liquid titanium measured by an electrostatic levitator. J Chem Thermodyn. 2019;131:557–62.
89. Deardorff DK, Hayes ET. Melting point determination of hafnium, zirconium, and titanium. JOM. 1956;8:509–10.
90. Lu L, Zhang S, Xu J, He H, Zhao X. Numerical study of titanium melting by high frequency inductive heating. Int J Heat Mass Transf. 2017;108:2021–28.
91. Gibbs GB, Graham D, Tomlin DH. Diffusion in titanium and titanium—niobium alloys. Philos Mag. 1963;8:1269–82.
92. Ishikawa T, Koyama C, Nakata Y, Watanabe Y, Paradis PF. Spectral emissivity and constant pressure heat capacity of liquid titanium measured by an electrostatic levitator. J Chem Thermodyn. 2019;131:557–62.
93. Teodorescu G, Jones D, PAO R, Guo B. High temperature emissivity of high purity titanium and zirconium. 2018;1–10.
94. Cezairliyan A. Radiance temperature of niobium at its melting point. J Res Nat Bur Stand Sect A Phys Chem. 1973;77A:333–40.
95. Pemsler JP. Thermodynamics of the interaction of niobium and tantalum with oxygen and nitrogen at temperatures near the melting point. J Electrochem Soc. 1961;108:744.
96. Schaefers K, Rösner-Kuhn M, Frohberg MG. Enthalpy measurements of undercooled melts by levitation calorimetry: the pure metals nickel, iron, vanadium and niobium. Mater Sci Eng. 1995;197:83–90.
97. Satya Prasad VV, Baligidad RG, Gokhale AA. Niobium and Other High Temperature Refractory Metals for Aerospace Applications. Springer, Singapore, 2017. pp. 267–88. doi:10.1007/978-981-10-2134-3_12
98. Balat-Pichelin M, Sans JL, Escape C, Combes H. Emissivity of elgiloy and pure niobium at high temperature for the solar orbiter mission. Vacuum. 2017;142:87–95.
99. Righini F, Spišiak J, Bussolino GC. Normal spectral emissivity of niobium (at 900 nm) by a pulse-heating reflectometric technique. Int J Thermophys. 1999;20:1095–106.
100. Malter L, Langmuir DB. Resistance, emissivities and melting point of tantalum. Phys Rev. 1939;55:743–47.
101. Rinnerbaur V, Senkevich JJ, Joannopuulos JD, Soljacic M, Celanovic I, Harl RR, Rogers BR. Low emissivity high-temperature tantalum thin film coatings for silicon devices. J. Vac. Sci. Technol. A. 2013;31:011501. https://doi.org/10.1116/1.4766295
102. Agte C, Alterthum H, Becker K, Heyne G, Moers K. Physikalische und chemische Eigenschaften des Rheniums. Zeitschrift für anorganische und allgemeine Chemie. 1931;196:129–59.
103. Cedillos-Barraza O, Manara D, Boboridis K, Watkins T, Grasso S, Jayaseelan DD, et al. Investigating the highest melting temperature materials: a laser melting study of the TaC-HfC system. Sci Rep. 2016;6:37962.
104. Hong Q-J, van de Walle A. Prediction of the material with highest known melting point from *ab initio* molecular dynamics calculations. Phys Rev B. 2015;92:020104.
105. Stanfield AD, Manara D, Robba D, Hilmas GE, Fahrenholtz WG. Measurement of the melting temperature of ZrB_2 as determined by laser heating and spectrometric analysis. J Am Ceram Soc. 2021;104:2780–87.
106. Scott HG. Phase relationships in the zirconia-yttria system. J Mater Sci. 1975;10:1527–35.

SUPPORTING INFORMATION

Additional supporting information can be found online in the Supporting Information section at the end of this article.

How to cite this article: Thorpe F, Li T, Weber R, McCormack SJ. Environmental conical nozzle levitator equipped with dual wavelength lasers. J Am Ceram Soc. 2023;1–14. https://doi.org/10.1111/jace.19542